The magnetosheath at high spectral resolution

K. D. Küntz[1,2]*, D. Koutroumpa[3], W. R. Dunn[4,5], A. Foster[6], F. S. Porter[2], D. G. Sibeck[2], and B. Walsh[7]

[1]The Henry A. Rowland Department of Physics and Astronomy, Johns Hopkins University, 3701 San Martin Drive, Baltimore, MD, 21218, USA;

[2]NASA Goddard Space Flight Center, 8800 Greenbelt Road, Greenbelt, MD 20771, USA;

[3]LATMOS-OVSQ, CNRS, UVSQ Paris-Saclay, Sorbonne Université, 11 Boulevard d'Alembert, 78280, Guyancourt, France;

[4]Department of Physics and Astronomy, University College London, London, UK;

[5]The Centre for Planetary Science at UCL/Birkbeck, Gower Street, London WC1E 6BT, UK;

[6]Center for Astrophysics, Harvard University & Smithsonian Institution, 60 Garden Street, Cambridge, MA 02138, USA;

[7]Center for Space Physics, Boston University, 110 Cummington Mall, Boston, MA, USA

Key Points:

- The proposed Line Emission Mapper (LEM) will allow observations of the solar wind charge exchange emission from the Earth's magnetosheath over its multi-year mission from its anticipated launch in 2032.
- LEM will observe small scale structure (+/−0.22 R_E) of small regions (3.7 × 3.7 R_E) of the magnetosheath at high cadence (3 minute), complementing SMILE's (Solar wind Magnetosphere Ionosphere Link Explorer) global imaging of the magnetosheath.
- LEM will produce high energy resolution (<2 eV) spectra of the charge exchange spectrum from the magnetosheath emission, providing abundance data for a wide range of solar wind species not covered by existing in situ measurements, and likely covering a large fraction of the solar cycle.

Abstract: While we eagerly anticipate SMILE's (Solar wind Magnetosphere Ionosphere Link Explorer) unprecedented X-ray observations of the Earth's magnetosheath and the initiation of a new era of magnetospheric research, it seems appropriate to look ahead to the abilities of the next generation of astrophysics missions. Of these, the Line Emission Mapper (LEM), a large aperture micro-calorimeter based mission, is currently planned to be able to observe the magnetosheath at high spectral resolution (~2 eV). With a field of view of ~30', LEM will allow higher spatial resolution and higher cadence measurement of the motion of a very small portion of the magnetopause over relatively short periods of time (multiple hours), complementing SMILE's global mapping. LEM's strength is its spectral resolution. It will be able to measure the abundance of a broad range of elements and ionization states, many of which are inaccessible to current in situ instruments, and will be able to separate the emission from the magnetosheath from the emission from the cosmic X-ray background using the difference in their relative velocities.

Keywords: magnetosheath; charge exchange; solar wind abundances

1. Introduction

Charge exchange is the process by which an ion encounters a neutral atom, the neutral loses an electron to the ion, and that electron drops from an excited state to a ground state, producing one or more photons. Charge exchange will occur anywhere a hot plasma has an interface with a cool neutral gas, such as supernova remnants near molecular clouds. Charge exchange with bare or hydrogenic ions produces X-rays and extreme ultraviolet photons, in the same lines that are often used for plasma diagnostics. In astrophysical contexts, the interfaces between hot plasmas and cool gas are very thin; the emission from the plasma itself tends to dominate over the charge exchange emission, so the plasma diag-

nostics are perturbed by only small amounts. Charge exchange emission is a powerful tool for understanding to what extent hot and cool components are mixed.

However, there is a foreground source of charge exchange emission: the highly ionized solar wind interacting with any neutral atom in the heliosphere. Those neutral atoms can be planetary atmospheres (Venus: Dennerl et al. (2002), Earth: Cravens et al. (2001), Mars: Dennerl (2002), Jupiter: Branduardi-Raymont et al. (2004), the Io torus: Elsner et al. (2002), possibly Uranus: Dunn et al. (2021), Pluto: Lisse et al. (2017), Comets: Lisse et al. (1996); Bodewits (2007), and the Moon: Collier et al. (2014)), which we generally refer to as producing magnetospheric emission. Those neutral atoms can also be the neutral interstellar medium that flows through the entire heliosphere, producing a relatively smooth, constantly varying X-ray background (Robertson et al., 2001; Koutroumpa et al., 2006) which can be extremely bright in the

helium focussing cone (Galeazzi et al., 2014). The bright foreground produced by the terrestrial magnetosphere and/or the nearby heliosphere remains a significant issue in understanding the diffuse emission from the Galactic halo and other astrophysical sources (Kuntz, 2019). Because charge exchange is both a powerful tool, and a severe nuisance in astrophysics, there has been significant interest in measuring the underlying atomic data (e.g., Beiersdorfer et al., 2003; Brown et al., 2009; Frankel et al., 2009; Leutenegger et al., 2013; Betancourt-Martinez et al., 2014, 2018; Zhang RT et al., 2022).

Ever since the distinct signature of solar wind charge exchange was seen in XMM-Newton spectra (Snowden et al., 2004), astrophysical missions and methods have been brought to bear on the problem of solar wind charge exchange (SWCX). The sounding rocket payload used to create the Wisconsin all-sky X-ray survey was repurposed to observe the helium focussing cone (Galeazzi et al., 2014). "Lobster-eye" optics, which had been developed for wide field of view imaging for a number of astrophysical missions, were proposed for a lunar observatory of the terrestrial magnetospheric charge exchange (Collier et al., 2009), and were flown on sounding rockets (Collier et al., 2015) to support larger proposals such as the subject of the current special issue, SMILE (The Solar wind Magnetosphere Ionosphere Link Explorer), which will be launched in May 2025[1]. Thus it should be no surprise that astrophysical missions are designed with a sensitivity to SWCX and the desire to use SWCX to address a wide range of astrophysical and heliophysical problems.

LEM is being proposed as a NASA Probe class mission concentrating on imaging spectroscopy (Kraft et al., 2022). Although it will be able to observe planetary atmospheres and surfaces, as well as comets, by far the brightest accessible SWCX target is the Earth's magnetosphere. The spectrum of the magnetospheric SWCX emission will be an ideal laboratory both for understanding a broad array of solar wind ion abundances and for checking the calculated charge exchange cross-sections. The solar wind ion abundances, in turn, feed back into our understanding of multiple fractionating physical processes at the base of the solar wind, and to solar abundances themselves. Imaging portions of the magnetosheath at scales inaccessible to any proposed wide-field imager will complement SMILE and its successors.

2. Mission Description

LEM will consist of a single instrument, a microcalorimeter at the focus of a grazing incidence mirror. The mirror will consist of many pairs of thin monocrystalline silicon shells coated with either Ir or Pt. The outer diameter of the mirror will be 1.5 m, which will allow an effective area of ~1600 cm^2 for a photon with E = 0.5 keV. The angular resolution will be ~15". The detector will cover a FOV of approximately 30' by 30'. Over the entire FOV the energy resolution will be better than 2 eV (2.5 eV requirement), while the central portion of the detector will have an energy resolution of at least 0.9 eV (1.2 eV requirement). LEM will be a substantial improvement upon XRISM which is scheduled to be launched into low Earth orbit in September 2023; XRISM will have

a resolution of 5−7 eV, a FOV of 3' by 3', and an effective area of only ~160 cm^2 for a photon with E = 1.0 keV.

The baseline orbit for LEM is a Lyapunov Quasi-Halo orbit at L1 with a period of six months. This orbit will allow a maximum elongation of the spacecraft from the Earth–Sun line of ~47° during four roughly month-long periods per year. From the maximum elongation, the line of sight is tangent to the magnetopause relatively close to the nose, as can be seen in Figure 1, which is a cross-section of the magnetosheath X-ray emissivity in the GSE-Z = 0 plane. Figure 2 shows the relative strength of the soft X-ray emission as seen from LEM when LEM is at its greatest elongation. The magnetopause, the sharp boundary between the outer magnetosheath (where solar wind charge exchange occurs) and the inner magnetosheath (where the absence of high charge state ions precludes that emission), is readily distinguishable, as are the northern and southern cusps, leading down from the magnetosheath towards the Earth's magnetic poles where connected terrestrial and solar wind magnetic field lines allow solar wind ions to penetrate deep into the magnetosphere and produce strong soft X-ray emissions as they encounter high exospheric neutral densities.

Figure 1 also demonstrates the problem of observing the magnetosheath from LEM 's minimum elongation; the line of sight strikes
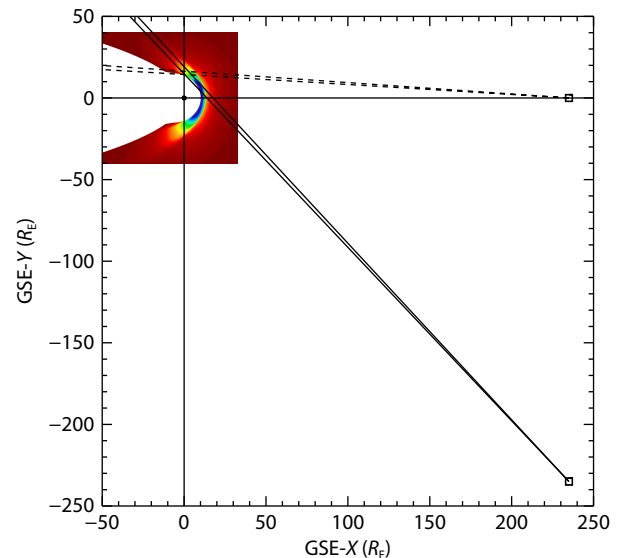

Figure 1. The relative configuration of LEM, the Earth, and the Earth's magnetosheath in the ecliptic plane. The Earth is at the origin while the inset image is a cross-section through a BATSRUS based model of the X-ray emissivity in the near-Earth environment. Two locations are shown for LEM. The two solid lines emanating from the box at GSE = (235, −235, 0) define a 30' FOV for LEM when it is at its greatest elongation; the line of sight has an extended path nearly tangential to the magnetopause through the brightest part of the magnetosheath. The two dashed lines emanating from GSE = (235, 0, 0) represent a line of sight from LEM when it is at L1; the line of sight through the magnetopause is relatively short. Details of the simulation are provided in Section 5.
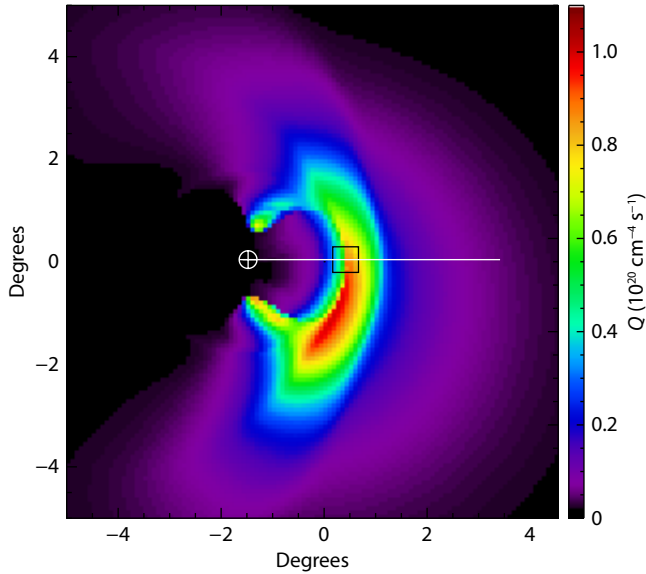
Figure 2. The relative SWCX emission as seen from the vantage point of LEM at its greatest elongation. The circle is the location of the Earth. The black box shows the size of the LEM FOV. The white line shows the location of the cut used in Figure 4. This simulation was for a median solar wind flux and happens to be for a northern hemisphere winter. Details of the simulation are provided in Section 5.

the magnetopause closer to the normal, so there is no sharp boundary. The pathlength through the magnetosheath is short, so the emission is weak. The magnetopause is also confused by the cusps, which are projected against the magnetopause near the poles.

From the spacecraft, 15" subtends 0.024 R_E at the Earth. However, given that exposure times will be driven by the time scales on which the magnetopause location varies, the effective resolution, due to the relatively low count rate, is much larger, as will be discussed below. The entire FOV subtends only ~3 R_E at the Earth.

3. Motivations

3.1 The Astrophysical Case

The LEM baseline capabilities allow observations of the Earth's magnetosheath, the brightest source of charge exchange emission. While the magnetosheath might not seem to be an obvious target of interest for astrophysics, it is the key to resolving a problem that has arisen over the last two decades. Astrophysicists are primarily interested in determining the physical state of emitting plasmas, determining whether they are in thermal equilibrium, overionized, underionized, or even photoionized. Each of these states can be diagnosed using line ratios, such as the triplet emitted by He-like O (e.g., Ness et al., 2001; Porquet et al., 2010). Temperatures are determined from the ratios of the strengths of lines from different charge states of the same species. However, if the plasma of interest is being observed through a region emitting via charge exchange, such as the entire heliosphere, then the line ratios from the astrophysical plasma become very uncertain indeed. Astrophysicsts have become frustrated because, for example, two observations of the same part of the Galactic halo at different times can produce vastly different results, depending upon the strength of the constantly varying foreground helio-

spheric charge exchange (e.g., Henley et al., 2007; Henley and Shelton, 2008).

Astrophysicists have been working with their colleagues in space physics, heliophysics, and planetary physics to characterize the charge exchange emission from the heliosphere and, since many X-ray observatories are in low Earth orbit, from the Earth's magnetosphere (See Kuntz (2019) for a first entrée into this issue.) This is a difficult problem since the charge exchange interaction cross sections are poorly measured, if they are measured at all. While great progress has been made towards measuring cross sections, existing measurements suggest that scaling between species is not always applicable (Leutenegger et al., 2010); much more laboratory measurement needs to be done. Further, the abundances in the solar wind of the various ions that can produce X-ray emission are sometimes poorly measured, and sometimes they have not been measured at all.

Figure 3 demonstrates one dimension of this problem. The left-hand plot shows the species expected in the solar wind, their expected contributions to solar wind charge exchange emission, and marks those species for which there are in situ measurements. The right-hand plot shows the species expected to contribute to the X-ray background spectrum. The color scale indicates the relative contribution of each species. There is considerable overlap between the two populations of ions! However, there are a number of ions that are either not measured or are poorly measured, that are likely to contribute strongly to the charge exchange spectrum, and that are key lines for understanding the abundances/thermal states of astrophysical plasmas.

Measurement of the charge exchange spectrum from the Earth's magnetosheath, even if only from the equivalent of a series of snapshots, will allow astrophysicists to construct an empirical model of solar wind charge exchange emission, and will allow verification of results from laboratory astrophysics. The observations, however, will serve more than astrophysics.

3.2 A Heliophysical Case

3.2.1 Solar wind

In situ measurements of abundances in the solar wind, is one leg of the triad, including spectroscopy and helioseismology, upon which the solar abundance is based. Each method has its own strengths, and it is through the combination of these techniques that we have come to understand, to some extent, the solar abundance. Of course, compared to the flow from polar coronal holes, the equatorial solar wind flow is not an ideal measure of the solar abundance because the abundances have been modified by multiple effects: first ionization potential (FIP) fractionation, mass fractionation, and the multiple processes that preferentially accelerate some ion species but not others (see the summary of von Steiger and Zurbuchen, 2016). Of what use then, are abundances from the streamer flow? The very processes that complicate the streamer abundances are themselves active fields of inquiry.

Matching abundances at the solar surface, observed through spectroscopy, with abundances measured in the solar wind is a key tool for understanding the FIP effect and gravitational settling. "Intermediate FIP" elements, such as C, P, and S will play a key role in understanding the underlying mechanisms, but S is not
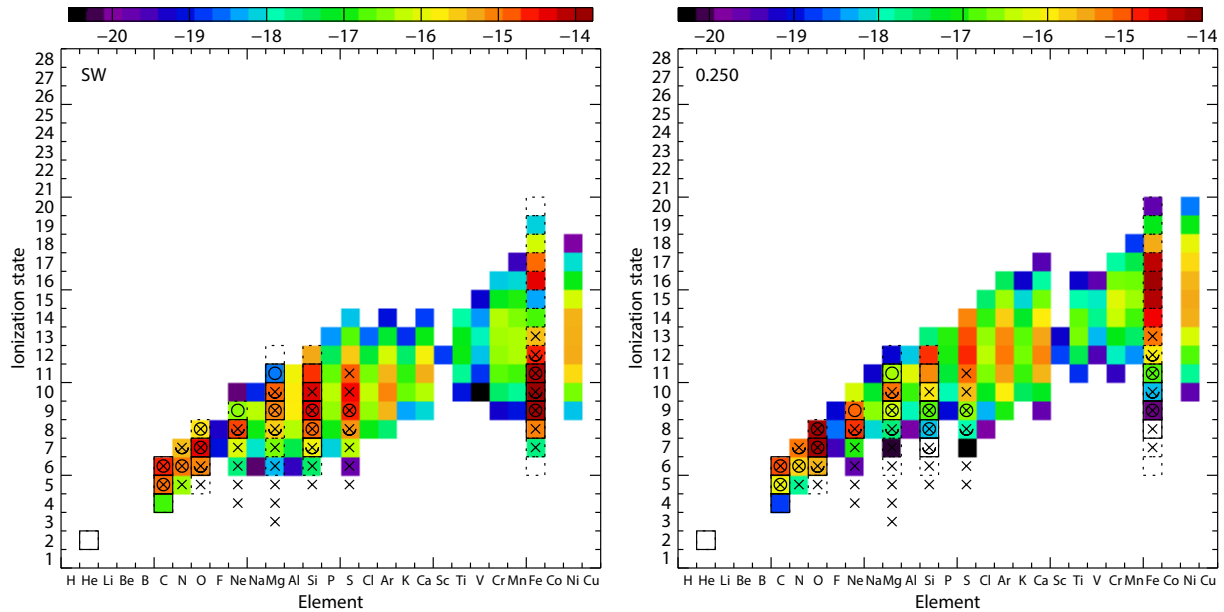
Figure 3. Left: The relative X-ray emission strengths of different charge states of different species in a slow solar wind. We have applied a linear fit to the freeze-in temperature as a function of atomic number from Gloeckler and Geiss (2007), used the freeze-in temperatures of a species to approximate the relative charge state populations, and then used the X-ray emissivities of those charge states within the LEM energy band in order to approximate the relative X-ray brightness of each species/charge state. These values were extracted from the APEC collisional ionization equilibrium model. The results should be viewed as merely illustrative! The boxes indicate ions measured by ACE while the "×" indicate ions measured by Ulysses (Schwadron and Cravens, 2000). Dashed boxes are species that are measured, but not well measured by ACE. The full circles indicate ions directly measurable by LEM as described in the text (Section 6.2.1) while the half circles are ions that should be measurable by LEM by spectral fitting. Note that we have not included most odd ions in our LEM simulation because they have not been measured in the solar wind by in situ experiments. Right: The relative X-ray emission strengths of different charge states of different species in an astrophysical plasma with $kT = 0.25$ keV. These were extracted from the APEC collisional ionization equilibrium model. The color code is the emissivity in the log of photons $cm^{-3} s^{-1}$.

routinely observed in the slow wind, and P is not observed at all with in situ measurements. Gravitational settling theory has relied on optical spectroscopy of multiple species, but some, such as S and Ar are not matched with solar wind measurements. These species will be accessible through X-ray observations of the magnetosheath with LEM. The relative abundances of different ions of a particular element reflect the ionization/recombination history of the ion before freeze-in, and constrain solar wind acceleration mechanisms (see Rivera et al., 2022, for a concise summary of these issues).

In situ experiments relying on the time-of-flight vs. energy technique (Gloeckler et al., 1992) have intrinsic biases; less abundant ions falling near more abundant ions are extremely difficult to separate. Spectroscopy brings measurements with a very different set of biases (weak lines near strong lines) which are likely to be much reduced since every ion produces multiple lines. Thus, LEM will expand the range of elements, and thus the range of masses and ionization potentials, available for study beyond those currently accessible by in situ instruments.

3.2.2 Magnetopause motion
Besides probing the composition of the solar wind for hitherto inaccessible species, LEM offers opportunities for higher angular

resolution studies of the magnetosphere, albeit over much smaller regions.

The Dungey cycle (Dungey, 1961) provides the organizational framework for understanding the interaction of the solar wind with the magnetosphere. On the dayside, the solar wind encounters the Terrestrial magnetic field, and we expect magnetic reconnection to occur that will link the outer part of Terrestrial field to the interplanetary magnetic field, allowing solar wind ions to enter the magnetosphere. As the solar wind sweeps past the Earth, those newly connected field lines are pulled back into the magnetotail, where the anti-aligned fields that bound the neutral sheet reconnect, energizing and accelerating the local ions back towards the Earth. This overly simplified picture provokes a number of questions.

We expect dayside reconnection to move the magnetopause Earthward. How local or global is that reconnection, and how does the effect of a local reconnection propagate to the rest of the magnetopause? Is the reconnection temporally continuous or episodic? Case studies suggest that all options can be observed, though what triggers any particular mode is unclear (see Sibeck et al., 2018, for a review). Part of the problem is that we cannot image reconnection, we can only observe its effects on the aurorae, for example, which does not provide an unambiguous local-

ization for the reconnection. Understanding the global reaction of the magnetopause to reconnection is, of course, the motivation for large field-of-view X-ray imagers such as the SMILE SXI, coupled to near-Earth solar wind monitors, allowing one to track both the solar wind impetus (in the general sense) and the reaction of the magnetopause.

The effects of nightside reconnection are yet more difficult to evaluate. Night side reconnection closes and returns magnetotail magnetic field lines to the dayside (Sibeck et al., 2022). After that reconnection, it is not clear on what temporal/spatial scales the global field changes. Of course, nightside reconnection also injects ions into the ring current, subsequently enhancing the magnetosphere field strength, and inflating the dayside magnetopause. Thus, the STORM team has proposed coupling the wide-field X-ray imager with an energetic neutral atom imager for simultaneous imaging of the ring current (Sibeck et al., 2018).

Although global imaging is the ideal, at the heart of this problem is the need for continuous measurement of the magnetopause distance (impossible with in situ measurements) which can then be correlated with the solar wind inputs, and a whole suite of ground- and space-based measurements. LEM can provide such monitoring spanning multiple hours, as 100 ks (~28 hour) observations are typical for X-ray astrophysics, and longer exposures (200–300 ks) are not unusual.

3.2.3 Bowshocks and foreshocks and structure

Earth's collisionless bow shock forms to allow the super-alfvenic solar wind to thermalize and be diverted around Earth's and its magnetosphere. This boundary provides a sharp delineation in the solar wind plasma density and thus SWCX. While the traditional MHD perspective is that the bow shock is a smooth boundary, a growing body of in situ spacecraft measurements and numerical models, including kinetic physics, present a boundary that is constantly reforming, developing ripples, waves, and kinetic structures (Schwartz and Burgess, 1991; Omidi et al., 2005; Hietala and Plaschke, 2013). The spatial scale of many of these structures are thought to be on the order of hundreds to thousands of km ($0.1-2\ R_E$) however the community has been unable to provide well-defined spatial scales. High angular resolution imaging of portions of the shock region with LEM could help address fundamental questions in shock formation and dynamics.

Upstream of a collisionless shock, incoming charged particles can be reflected by electromagnetic waves and returned upstream, forming a turbulent and dynamic foreshock region. Although spacecraft have made in situ measurements to quantify local waves and particle behavior (Gosling et al., 1978; Paschmann et al., 1980), spatial properties and dynamics are more challenging with in situ probes. The only images of this region to date have been composed slowly in energetic neutral atoms (ENA) with a 9-year exposure (Dayeh et al., 2020). The ENA measurements provide valuable maps of large trends, however there are many physical processes occurring on shorter time scales. Since the plasma temperature in the foreshock is higher than that in the surrounding

regions of the solar wind, the collisional frequency will be higher and will generate more X-rays through SWCX. Maps of the spatial extent of the foreshock during different driving conditions generated by scanning the LEM FOV through the approppriate region would provide valuable information on how particles are scattered at the shock.

The foreshock is also the formation site for a number of dynamic kinetic phenomena such as hot flow anomalies, foreshock bubbles, and density holes, each of which exhibit plasma heating, spatially sharp changes in solar wind density, and can be a number of Earth radii in size. With a high collecting area from LEM these could be imaged within the mission's FOV. Some of these structures have also been observed to displace a portion of the bow shock and magnetopause by as much as 5 R_E in the sunward direction as they travel downstream after formation and persist for minutes (Sibeck et al., 1999; Jacobsen et al., 2009). Understanding the spatial extent of these features is critical for measuring the impact they have on depositing energy into Earth's magnetosphere and the generation of space weather.

3.2.4 Cusp science

The opportunities to study the cusps are not so clear. The cusps are closer to the Earth, 1° to 1.5° (even when LEM is at L1 and closer to the Earth), and the Earth is X-ray bright due to reflected solar X-rays and atmospheric fluorescence. The extent to which the quality of the optics will reduce the stray light problem and allow cusp observations is not yet known. However, imaging the width of the cusp, and determining the extent to which it is uniformly filled with charge exchanging ions is important to understanding the transfer of the solar wind ions from the surface of the magnetosphere through the cusps to the atmosphere.

4. Some Considerations

Since LEM is designed as a flexible multi-purpose astrophysical observatory, its design is not customized for our observations. However, LEM is still very well suited for these observations. Here we consider how and when the observations might be made.

4.1 FOV

As noted above, the FOV is relatively small. Given that the magnetopause moves a significant amount as the solar wind varies, we need to determine by how much the typical motion of the magnetopause places it outside the FOV. Figure 4 shows a profile of the emission along the white line shown in Figure 2. In addition to a cut through the simulation shown, which has $nv = 2.41 \times 10^8$ cm^{-2} s^{-1}, a median solar wind flux[2], we also show the profile for solar wind fluxes at the 25th percentile, the 75th percentile, and the 92nd percentile. From this vantage point, the magnetopause moves about 20′ from the 25th to the 92nd percentile. Since we will not know a priori where the magnetopause will be for any particular observation, a single stationary pointing will not be guaranteed to contain the location of the magnetopause. However, LEM is being designed to be very nimble, so it will be able to "nod" back and forth across the nominal magnetopause location in

---

[2] The statistics of the solar wind flux was taken from the OMNI database over the last two solar cycles.
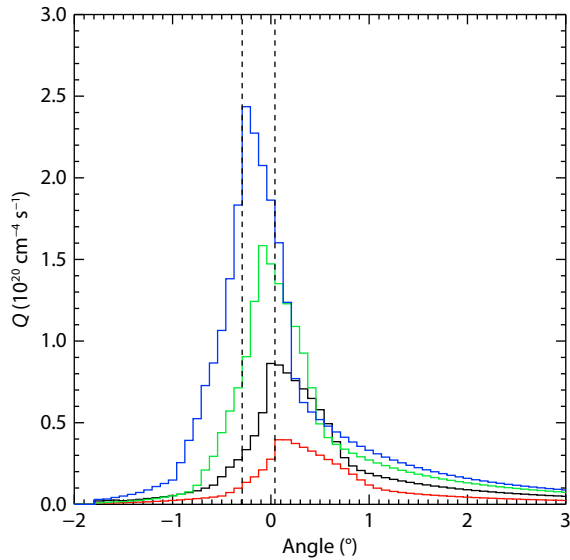
Figure 4. A cut through the magnetosheath along the white line shown in Figure 2. Each profile shows Q, which is proportional to the relative emission along the white line in Figure 2 for a different solar wind flux. We have chosen the location of the magnetopause for the lowest solar wind flux as the reference point. All profiles are extracted from simulations as described in Section 5. The red line is for a 25th percentile flux (1.48×10^8 cm^{-2} s^{-1}), the black line is for a median solar wind flux (2.31×10^8 cm^{-2} s^{-1}, the green line is for a 75th percentile flux (3.18×10^8 cm^{-2} s^{-1}), and the blue line is for a 92nd percentile flux (5.00×10^8 cm^{-2} s^{-1}). The dashed lines show the difference in magnetopause location between the 25th and 92nd percentile fluxes, 20′.

order to build up a broader image that is sure to include the magnetopause. Thus, the uncertainty in the location of the magnetopause will not preclude us from getting a good image of it.

4.2 Backgrounds

For the baseline orbit, the Earth, as seen by LEM, will always be on the ecliptic. Figure 5 shows the ROSAT All-Sky Survey (RASS) at $\frac{1}{4}$ keV and $\frac{3}{4}$ keV remapped into ecliptic coordinates; the ecliptic is the horizontal center line. The bright emission to the right in the $\frac{3}{4}$ keV map, which we would clearly wish to avoid, is the Galactic center; the Earth will appear there only during northern hemisphere summer. The opposite side of the sky is relatively dim and relatively smooth, though there are still regions that should be avoided. Thus, LEM will be able to observe the magnetopause in periods when northern hemisphere aurora observatories are active, allowing for a great deal of coordination with other magnetospheric observing assets.

Although LEM will be performing an all-sky survey, the LEM−ASS, and thus can provide a spectrum at any point in the sky, the LEM−ASS will have a coverage of only 10 s at each location after the first year of operation, and a coverage of perhaps 100 s by the end of the mission. Thus, it will be important to observe the same part of the sky occupied by the magnetosheath a month or so before or after the magnetosheath observation in order to have a

suitable spectrum of the background.

4.3 GO and TOO Observations

Since LEM is an astrophysics mission where 70% of the observations are guest observer driven, users will be able to propose competetively for observations. It should be kept in mind that typical X-ray astrophysics guest observer (GO) proposals request ~100 ks (roughly 28 hours), so a successful proposal is likely to stare at the magnetopause for a relatively limited time in any particular proposal cycle. The minimum lifetime is five years, and the mission is expected to survive for much longer, so there is the likelihood of sampling the solar wind over a substantial portion of a solar cycle.

LEM will also support target of opportunity (TOO) proposals, which allow an observer to trigger an observation based on pre-set criteria, where the observation is made 48 hours (or longer if specified) after the trigger. Thus, it will be feasible to watch the magnetopause response to some coronal mass ejections.

5. Simulations

Given the above motivations for LEM observations of the Earth's magnetosheath, and the rather minimal constraints placed by the considerations of the previous section, we now consider the construction of simulations with which we can evaluate the feasibility of LEM observations of the magnetosheath.

The flux due to an atomic transition j due to charge exchange between a neutral of species k and a solar wind ion of species s and charge state q is given by

$$F_j = \int_0^\infty n_{neut} n_p v_{rel}\ \sigma_{ksq}(v_{rel}) b_{sqj} \frac{n_{sq}}{n_p}\ d\Omega dl/4\pi, \qquad (1)$$

where the integral is along the line of sight from the observer. The n_{neut}, n_p, n_{sq} are the densities of the neutral targets (mostly H for the exosphere), the solar wind protons, and solar wind ions
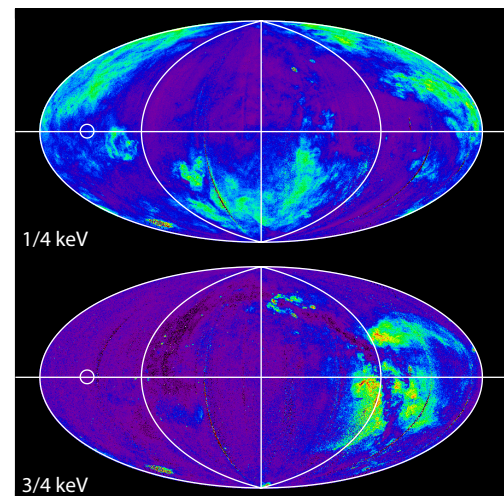

Figure 5. The ROSAT All-Sky Survey (Snowden et al., 1997) transformed into ecliptic coordinates (λ, β). The ecliptic is the horizontal line, while $\lambda = 0°$ is at the center. The circle is our sample of a typical background. Top: The RASS at $\frac{1}{4}$ keV. Bottom: The RASS at $\frac{3}{4}$ keV.

Küntz KD et al.: The magnetosheath at high spectral resolution

respectively. The σ_{ksq} is the cross section of the ion with neutral target k as a function of a relative velocity v_{rel}, while b_{sqj} is the probability that, having had a charge exchange interaction, that the resulting cascade produces the line j. The relative velocity of the ions and the neutrals, v_{rel} is given by

$$v_{rel} \sim (v_r^2 + v_t^2)^{\frac{1}{2}}, \tag{2}$$

where the v_r is the bulk velocity of the ions with respect to the neutrals, while v_t is the thermal velocity of the ions, generally $\sqrt{(3kT/m_p)}$. For convenience, we define

$$Q \equiv \int_0^\infty n_{neut} n_p v_{rel} \, d\Omega dl/4\pi, \tag{3}$$

where Q is in $cm^{-4}s^{-1}$. The emission along the line of sight is then the integral of F_j over all transitions that fall within the energy band of interest. Thus, if

$$\varsigma_{sqj} \equiv \sigma_{ksq}(v_{rel})b_{sqj}\frac{n_{sq}}{n_p}, \tag{4}$$

then

$$F = Q \sum_{sqj} \varsigma_{sqj}, \tag{5}$$

and thus Q, in the figures here, can be thought of as being instantaneously proportional to the X-ray emission.

For each pixel (line of sight) of our simulations the n_p, v_p, and T_p were extracted from a BATS-R-US (Tóth et al., 2005) model constructed with the "runs on demand" service of the NASA CCMC. Unless otherwise noted, the free-flowing solar wind proton density and velocity was fixed to 5.3 cm^{-3} and −402 km/s respectively. We have assumed a southward interplanetary magnetic field. The n_{neut} was extracted from a standard model of the inner exosphere (Hodges, 1994) that was extrapolated to greater distances with a $(R/R_E)^{-3}$ law. Thus, for each pixel we can extract from these two models the information required to construct Q. Figure 2 shows Q as a function of position as seen by LEM at its greatest elongation.

To convert Q to an X-ray count rate we use the slow solar wind spectrum from Koutroumpa (2007) and the magnetospheric SWCX production factor ($\sum_{sqj} \varsigma_{sqj}$) extracted from the ROSAT long-term enhancement (LTE) data by Kuntz et al. (2015). The slow solar wind spectrum is particularly apt as LEM is expected to be launched in 2032, which will be during a solar minimum. The Koutroumpa spectrum was constructed from the abundances of Schwadron and Cravens (2000) and the atomic data calculated by Karchenko (discussed to some extent in Kharchenko and Dalgarno, 2001), as described in Koutroumpa (2007). Less abundant species, such as P, Ar, or Ca have not been included, though they will be of interest. The cross sections and branching ratios were carefully curated for the purpose of SWCX studies, but this method has its limitations. Other models exist, such as ACX2 (Smith et al., 2012, and see http://www.atomdb.org/CX/) and within SPEX (Gu LY et al., 2016) which use very different assumptions about the distribution of quantum levels n and ℓ that are populated as a function of velocity, as well as the branching ratios for the subsequent cascade. The codes produce rather different spectra for anything except H-like, He-like, and possibly Li-like ions. Comparison of the

codes with one another and with laboratory measurements is beyond the scope of this work. Thus, our SWCX spectra can be considered "representative". The new implementation of the SWCX spectra by Koutroumpa (this volume) changes spectral details, but not to any great significance for our purposes.

Kuntz et al. (2015) used the relation between the LTE emission seen by ROSAT and the solar wind flux, as well as a mean relation between the Q along a ROSAT-like line of sight and the solar wind flux to construct a relation between Q and the ROSAT emission. The ROSAT $\frac{1}{4}$ keV LTE data are particularly useful as they were extracted from the R12 band (roughly 0.11–0.284 keV) which contains a large fraction of the SWCX emission. It should be noted that the ROSAT data were collected in 1990, during solar maximum, and we have not attempted to correct for the difference between the solar winds observed by ROSAT and a "standard" slow solar wind.

From Kuntz et al. (2015) we know that the ROSAT R12 band count rate is $(3.86 \pm 0.20) \times 10^{-20}$ count deg^{-2} cm^4 Q. For any SWCX spectrum with an arbitrary normalization, we can use the convolution of the spectrum by the ROSAT response to determine a new normalization, N, that produces 3.86×10^{-20} R12 band count s^{-1} deg^{-2}. Then, the LEM spectrum can be obtained by convolving the spectrum with the LEM response and multiplying by NQ. Thus, the overall flux is firmly anchored to ROSAT observations, while the accuracy of the individual line strengths depends upon the relative accuracy of the atomic data that was used to construct the spectrum.

The cosmic X-ray background is composed of emission due to the unabsorbed Local Hot Bubble (LHB), at least two Galactic halo components, and the unresolved cosmic background. The temperature of the thermal emission from LHB was taken from Bluem et al. (2022), while the normalization was taken from Snowden et al. (1998), corrected for heliospheric SWCX emission by Liu et al. (2017). The temperatures of the Galactic halo components were taken from Bluem et al. (2022) while the normalizations of those components were derived from HaloSat (Kaaret et al., 2019) data towards $(\ell, b) = (212.716°, +38.165°)$ which is equivalent to $(\lambda, \beta) = (135.2°, +0.3°)$, a rather typical region for which the temperatures of the halo components is particularly well characterized. The thermal emission was calculated using the collisional ionization equilibrium model APEC (Astrophysical Plasma Emission Code, Smith et al., 2014) with solar abundances. (Though not all of the Galactic halo components are expected to have solar abundances, the abundances and the normalizations are strongly anti-correlated, so little is lost for our purposes by fixing the abundances. In any case, while the fit may not be entirely physical, it represents the measured spectrum, and its flux, quite closely). The unresolved cosmic background was modeled as a power law with an index of 1.45 and a normalization of 10.9 keV cm^{-2} s^{-1} sr^{-1} keV^{-1} at 1 keV (Cappelluti et al., 2017), though this may not be entirely correct at lower energies (Gilli et al., 2007). For the purposes of this simulation we have assumed that the Local Hot Bubble and Galactic halo emission have minimal velocity with respect to the Earth. The parameters are given in Table 1. The SWCX/(cosmic + instrumental backgrounds) for LEM observations

Table 1. LEM background parameters.

Component	Function	Parameter
Instrumental	constant	1 count keV^{-1} s^{-1}
Local Hot Bubble	apec	kT = 0.084 keV, EM = 2.257 × 10^{-3} cm^{-6} pc
Galactic Halo	tbabs (apec)	$N(H)$ = 3.1 ×10^{20} cm^{-2}, kT = 0.166 keV, EM = 4.132 × 10^{-3} cm^{-6} pc
Hard Gal. Halo	tbabs (apec)	$N(H)$ = 3.1 × 10^{20} cm^{-2}, kT = 0.69 keV, EM = 4.151 × 10^{-4} cm^{-6} pc
Cosmic X-ray Bkg	tbabs (apec)	$N(H)$ = 3.1 × 10^{20} cm^{-2}, Γ = 1.45, N = 10.91 keV cm^{-2} s^{-1} sr^{-1} keV^{-1}

of the Earth's magnetosheath is roughly 0.64 in the 0.1−1.0 keV bandpass, though that will vary with bandpass.

6. Feasibility

Given its 25.5° × 15.5° FOV, SMILE will produce images of the global shape and structure of the magnetosheath. It will image the entire magnetosheath at a 5−10 minute cadence, allowing one to measure the global movement of the magnetopause of 0.25 to 0.5 R_E, depending on the strength of the solar wind. The SMILE spectral capabilities will be modest with an expected energy resolution of ~50 eV that is typical of CCD detectors.

Given the large extent of the magnetosphere, the small extent of the LEM FOV (30′), and the highly dynamic nature of the magnetosheath, LEM will not map the magnetosheath. LEM will be able to map the magnetosheath only by rastering the FOV over a ~4° × 6° region, and by the time LEM finishes a raster, the solar wind may have changed substantially. However, LEM can produce much higher resolution images of a smaller portion of the magnetosheath. LEM's strength will be measuring the spectrum of the SWCX emission, diagnosing the ion abundances of the solar wind.

6.1 SMILE-type Science

Figure 6 shows a simulated image of an stationary magnetopause built up over a three minute exposure during which the LEM FOV was "nodded" or scanned a distance of four FOV widths perpendicular to the GSE-Z direction, as shown by the white line in Figure 2. Even a vertical extent of ±15′ is enough to show a small amount of curvature in the magnetopause. We have ignored that curvature in creating the profile across the magnetopause shown in the lower panel of Figure 6.

How well can LEM determine the location of the magnetopause, the sharp break to the left of the peak in the profile? We assume that we have a relatively accurate profile of the magnetosheath, either through MHD models or through co-aligned and stacked images from a longer exposure. We used a ±14′ wide region of the model profile surrounding the peak, and we cross-correlated the model with the data to find the location with the best agreement. A Monte Carlo test with 1000 trials shows that the uncertainty in the location found by this method is ±1.32′ pixels, or ±0.22 R_E. Note that this is the uncertainty for a 3 minute exposure for a median solar wind flux of 2.13×10^8 cm^{-2} s^{-1}. We will do substantially better for higher solar wind fluxes, as the magnetopause is pushed deeper into the exosphere and the X-ray emissivity increases. This is substantially better than SMILE will be able to achieve (Sembay et al., 2024).

We note that the vignetting is likely to be better than what is shown since it is likely that the spacecraft will slow before reversing, thus increasing the exposure time at the ends of the image. Thus, it is likely that one could nod over a shorter distance to achieve the same unvignetted FOV.

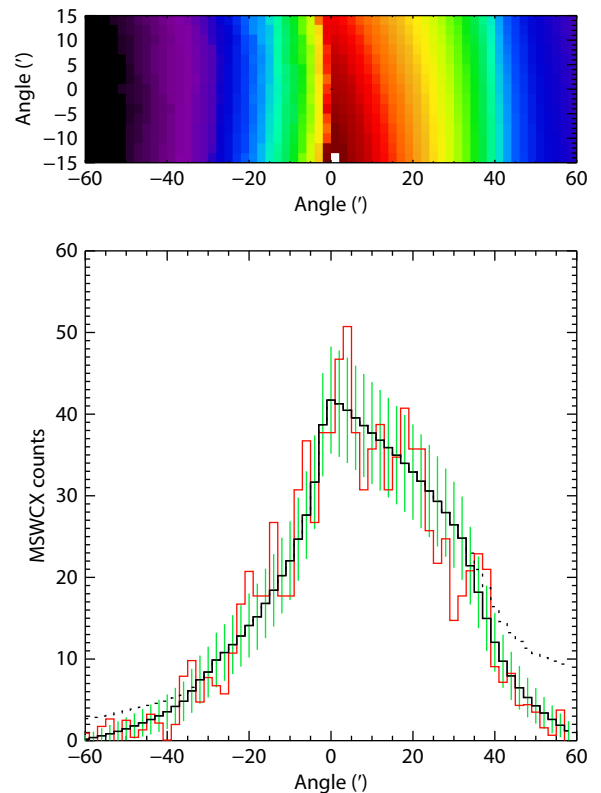The choice of a three minute observation is important. In the

Figure 6. Top: A simulated image of an immobile magnetopause created by scanning the LEM FOV a distance of three FOV widths in three minutes. No noise or background has been added to this image for clarity. The energy band of this image is 0.1−1.0 keV. The vignetting due to nodding has not been applied to this image. The image has 2′ pixels. Bottom: A profile of the magnetopause extracted from that image by summing along the pixel (2′ wide) columns of the above image. The dotted line shows the true magnetopause profile, before the effects of the scanning induced vignetting. The green lines show the uncertainty, including that due to the relatively smooth background. In red is a simulation of the profile with noise after the subtraction of the cosmic background, and including the noise due to the cosmic background.

Küntz KD et al.: The magnetosheath at high spectral resolution

extended STORM white paper (see Fig. 66 of Sibeck et al., 2018), we considered the fraction of time periods of a given length for which the movement of the magnetopause, $\Delta R_{MP} < 0.2$ R_E. For a median solar wind flux (a median R_{MP}), greater than 50% of 3 minute time periods have quasistationary magnetopause positions, i.e., half of our three minute scans will see magnetopause movement that is smaller than our uncertainty. As the solar wind flux decreases, the fraction of quasistationary times does grow, though slowly. Thus, we have an uncertainty small enough to be of interest extracted from a time short enough that the magnetopause has a good probability of being stationary.

6.2 Spectral Studies

It is difficult to stress sufficiently the transformative nature of microcalorimeter spectroscopy. Figure 7 demonstrates the difference between SMILE and LEM spectra. For this simulated spectrum we have assumed an observation of the brightest 30′ by 30′ region of the magnetopause and accumulate a very modest 10 ks (2.8 hours) of data. Figure 7 demonstrates the spectrum that we will observe, divided into instrumental background, cosmic background, and the magnetospheric SWCX. We also indicate the fraction of the total flux in each bin that is due to the magnetospheric SWCX emission.

As noted above, the SWCX spectrum shown in the figure should be considered "representative". It should also be noted that, no matter the issues with this (or any) SWCX spectrum, the SWCX emission dominates the background from below 0.2 keV to roughly 0.5 keV (where it can be seen to have many of the same features as the cosmic background spectrum), as well as many of the strong line complexes at higher energies.

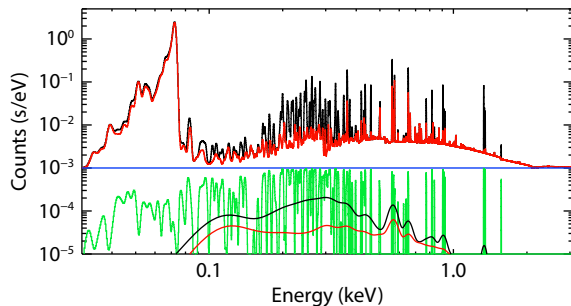Because the microcalorimeter line spread function (LSF) is domi-

Figure 7.   A comparison of the total spectra observed by LEM (upper black curve) including the magnetosheath for a median solar wind and all of the background emission components (upper red curve), as well as the anticipated instrumental background (blue curve). The spectrum has been convolved with the LEM response and line spread functions. The required LEM bandpass is 0.07−2.0 keV while the expected LEM bandpass is 0.05−2.5 keV. The green curve is the ratio of the magnetospheric component to the total spectrum, shifted downwards by a factor of 1000. The SMILE SXI spectrum (lower black and red curves) has been constructed for the same spectrum and emission region but does not include a instrumental background. The resolution of the SMILE spectrum is typical of that achieved by CCD-based X-ray instruments. The SMILE spectrum is on the same scale as the LEM spectrum.

nated by a Gaussian core with an extremely low wing to lower energies, we have the ability to measure the line center to an accuracy that is better than a energy resolution element. Monte Carlo simulations of individual lines suggest that the uncertainty in the line center, at 650 eV, is roughly 50(100) km/s for a line with 1000(100) counts.

6.2.1 Solar wind abundances

Bodewits (2007) demonstrated the ability to use X-ray spectra of comets to determine relative solar wind abundances using the relatively low energy resolution ($E/\Delta E$ ~10) ACIS CCD detectors on Chandra. The results depended on a model of the emission from 33 lines from six different ions (C V, C VI, N VI, N VII, O VII, O VIII) based on theoretical velocity-dependent cross sections. The LEM microcalorimeter will have $E/\Delta E$ ~500, and will produce direct measurements, independent of models, for a much broader range of ions.

The magnetospheric spectrum has been constructed using the measured solar wind abundances from Schwadron and Cravens (2000). Figure 3 shows the ions that we expect contribute to the charge exchange emission in the LEM X-ray band, as well as those ions that have been measured by in situ observations.

We have also marked the ions that will be easily accessible to LEM: species that have at least one line that produces greater than 50% of the flux at that line energy. For a 10 ks exposure, this equates to roughly 1000 counts or more in the charge exchange line. With such statistics one will be able to measure the line strengths directly, by summing the number of counts over the width of the line spread function after having subtracted the background spectrum from the magnetosheath spectrum. We have also marked the ions that will be moderately accessible to LEM: species that produce at least one line that produces more than 20% of the flux at that line energy. For a 10 ks exposure, this equates to roughly 100 counts or more in the charge exchange line. Here, the line strength will need to be measured by fitting a small energy band containing both the charge exchange and the background lines, and fitting the magnetospheric observation simultaneously with the background observation. A weaker species can also be extracted by fitting all of the sections of the spectrum containing its lines, but this will probably require fitting multiple charge exchange species as well as the background. Extracting the weaker species will not be trivial, but fitting complex spectra has been a regular procedure for X-ray grating spectroscopists for at least two decades.

This simulation elides the fact that the species and charge state abundances accessible to Ulysses or ACE are merely a subset of the ions expected in the solar wind. The odd-numbered species (Na, Al, P, etc.) do have lower abundances than their even-numbered brethren, but they are still present, and should be detectable with LEM. We have not included them in the LEM predictions as we have no abundance data with which to predict their strength.

Given the strength of magnetospheric charge exchange during CME events observed by XMM-Newton and Suzaku, and the very rich spectra already observed (e.g. Carter et al., 2010; Ishi et al.,

2019), albeit at far, far lower spectral resolution, a LEM spectrum of the magnetosheath taken during a CME event will provide a veritable banquet of lines. Beyond CME, we will be able to distinguish the abundance differences between slow and fast solar winds, was well as to explore the abundance differences between different structures in the solar wind, such as corotating shocks.

6.2.2 Velocity structure of the magnetosheath?

Given the high spectral resolution of LEM, it is tempting to consider the extent to which the velocity of the ions in the magnetosheath might produce perceptible line shifts and perceptible line broadening. Both shifting and broadening would provide more tools with which to separate the magnetospheric emission from the background and could provide diagnostics about the location and/or the velocity of the emission within the magnetosheath.

We should first note that the velocity structure along the LEM line of sight through the magnetosheath is complex, and varies strongly with position. As can be seen in Figure 8, a typical LEM LOS samples an extended path through the magnetosheath, along which both the X-ray emissivity and the velocity vary strongly. Each curve in Figure 9 shows the amount of emission at each velocity, while the different curves represent different lines of sight through the magnetosheath, from 10′ on the Earth side of the peak emission to 40′ from the peak emission away from the Earth. Each curve represents the shape of an emission line, the intrinsic line profile, from the magnetosheath, showing both how the emission is red-shifted to lower energies, and how part of the emission is shifted into a less red-shifted tail.

At the peak of the magnetosheath emission, a line of sight tangent to the magnetopause, one sees a two horned profile where the higher velocity peak is from emission moving tangent to the magnetopause, more parallel to the line of sight. The highest
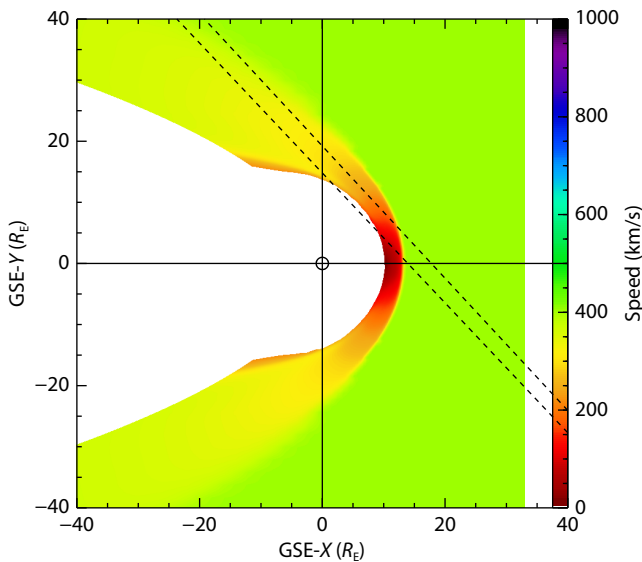
Figure 8. A map in the GSE *XY* plane of the velocity of the solar wind flowing through the magnetosheath. The pair of dashed black lines represent a 30′ wide LEM FOV from LEM at its greatest elongation. Details of the simulations are provided in Section 5.
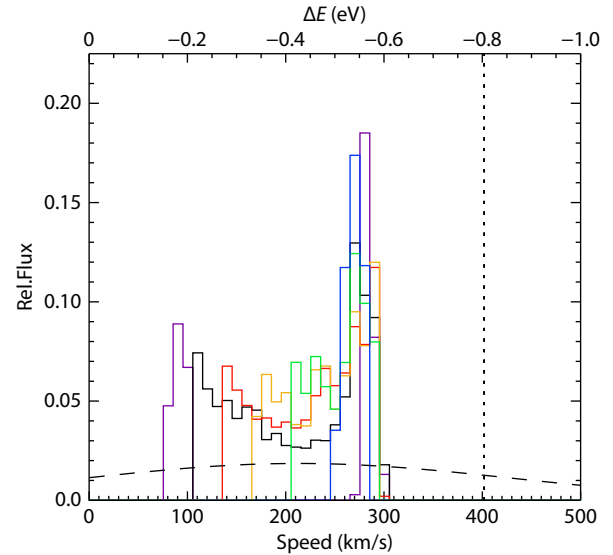
Figure 9. The relative amount of emission as a function of velocity along an infinitely narrow line of sight, for six different lines of sight. The lower axis shows the velocity while the upper axis shows the redshift in eV. These lines of sight were extracted from the median solar wind simulation. The black curve is for a line of sight at the peak of the emission, the lower dashed line in Figure 8. The purple curve is for a line of sight 10′ closer to the Earth, while the red, orange, green, and blue curves are for successive 10′ steps further away from the Earth. The dotted line shows the velocity of the free-flowing solar wind. The solid lines are the intrinsic line profile while dashed line shows the convolution of that profile with the higher resolution LEM line spread function.

velocities are typically ~75% of the free-flowing solar wind speeds. The lower velocities are produced by material moving more perpendicular to the line of sight. Moving the line of sight outward removes the lower velocity components. This simulation demonstrates that summing the spectrum over the whole LEM FOV would produce a very complex line feature, if we have the resolution to see it.

From the OMNI database, the 75th percentile for solar wind speed is ~490 km/s which would produce a maximum ~370 km/s along the line of sight. At the OVII(O VIII), 0.560(0.650) keV line, arguably the strongest SWCX lines, this velocity would produce a shift of 0.69(0.80) eV which is a significant fraction of an energy resolution element. Thus the center of the magnetospheric lines will be readily distinguishable from background lines due to the LHB at ~20 km/s, the flow speed of local interstellar medium. The velocity shift of the Galactic halo lines is a matter of inquiry; the bulk of the emission is thought to be near the Galactic disk (Kaaret et al., 2020), and to be due to gas streaming out of the disk, but the velocity with which it is streaming is unknown.

Much of the emission in the line, however, will have much smaller shifts, as can be seen from Figure 9. From these simulations we find that, for a FOV that has been set to maximize the magnetospheric emission ~50% of the emission is in the narrow, high velocity horn, and the remainder is smeared over ~0.3 eV. Once we convolve the intrinsic line profile with the instrumental line

spread function (and here we use the better, 0.9 eV resolution) we see that the line center is at ~210 km/s, roughly half the free-flowing solar wind speed. The resulting line is still broader than a line at a single velocity, and is asymmetric. This analysis, however, ignores thermal broadening in the shocked gas of the magnetosheath. Typical thermal velocities in the nose of the magnetosheath are a few million degrees. (This depends, of course, on the ions having a temperature similar to that of the protons, which is a matter of some study.) A few million degrees is also a typical temperature for the local hot bubble (10^6 K, which produces a broadening of 0.14 eV at 650 eV), the Galactic halo ($\sim 2 \times 10^6$ K), and the hard Galactic halo ($\sim 8 \times 10^6$ K), so the thermal broadening of the magnetosheath emission will be similar to that of the background emission.

Thus, while there is only a low probability that the gross velocity structure of the magnetosheath emission might be teased out of these observations, understanding the velocities of the emitting gas is important for understanding the extent to which and the ways by which the magnetospheric emission may be separated from the background.

7. Summary

The Earth's magnetosheath provides the brightest SWCX emission available. Exposures of roughly 10 ks that "nod" back and forth across the expected magnetopause location, will allow a more precise localization of the magnetopause as a function of the solar wind dynamics, may allow study of small scale structures at the magnetopause, and may allow study of the fainter emission from the foreshock. Several such exposures can be made over the course of a year, and a mission launch in 2032 will allow observations to begin at solar minimum and continue towards solar maximum. LEM will address many of the compelling science questions that motivate SMILE, but LEM will not address the global questions that SMILE addresses.

These observations, coupled with similar or shorter exposures of the same patch of sky taken a few months before or after, will provide strong spectra of the magnetosheath with a wealth of lines. Spectroscopy will allow access to species not covered with current in situ abundance measurement, and repeated observations will allow abundance measurements as a function of the solar wind speed and type. The velocity shift of the lines will allow better separation of the SWCX emission from the cosmic X-ray background.

While astrophysicists will use these data to better characterize and remove the SWCX component from observations of cosmic objects, laboratory astrophysicists will use these data to diagnose the deficiencies of our spectral codes, as well as identify crucial lacunae in laboratory measurement. Those who are interested in the composition of the solar wind (and by extension, the Sun) will find a wealth of data that will allow access to even less abundant species as the total exposure increases. Finally, LEM magnetospheric studies will be complementary to that produced by SMILE.

Acknowledgments

References

Beiersdorfer, P., Boyce, K. R., Brown, G. V., Chen, H., Kahn, S. M., Kelley, R. L., May, M., Olson, R. E., Porter, F. S., … Tillotson, W. A. (2003). Laboratory simulation of charge exchange-produced X-ray emission from comets. *Science*, *300*(5625), 1558–1559. https://doi.org/10.1126/science.1084373

Betancourt-Martinez, G. L., Beiersdorfer, P., Brown, G. V., Kelley, R. L., Kilbourne, C. A., Koutroumpa, D., Leutenegger, M. A., and Porter, F. S. (2014). Observation of highly disparate *K*-shell x-ray spectra produced by charge exchange with bare mid-*Z* ions. *Phys. Rev. A*, *90*(5), 052723. https://doi.org/10.1103/PhysRevA.90.052723

Betancourt-Martinez, G. L., Beiersdorfer, P., Brown, G. V., Cumbee, R. S., Hell, N., Kelley, R. L., Kilbourne, C. A., Leutenegger, M. A., Lockard, T. E., and Porter, F. S. (2018). High-resolution charge exchange spectra with l-shell nickel show striking differences from models. *Astrophys. J. Lett.*, *868*(2), L17. https://doi.org/10.3847/2041-8213/aaef82

Bluem, J., Kaaret, P., Kuntz, K. D., Jahoda, K. M., Koutroumpa, D., Hodges-Kluck, E. J., Fuller, C. A., LaRocca, D. M., and Zajczyk, A. (2022). Widespread detection of two components in the hot circumgalactic medium of the milky way. *Astrophys. J.*, *936*(1), 72. https://doi.org/10.3847/1538-4357/ac8662

Bodewits, D. (2007). Cometary X-rays. Solar wind charge exchange in cometary atmospheres. Groningen: University of Groningen.

Branduardi-Raymont, G., Elsner, R. F., Gladstone, G. R., Ramsay, G., Rodriguez, P., Soria, R., and Waite, J. H. Jr. (2004). First observation of Jupiter by *XMM-Newton*. *A&A*, *424*, 331–337. https://doi.org/10.1051/0004-6361:20041149

Brown, G. V., Beiersdorfer, P., Chen, H., Clementson, J., Frankel, M., Gu, M. F., Kelley, R. L., Kilbourne, C. A., Porter, F. S., … Wargelin, B. J. (2009). Studies of X-ray production following charge exchange recombination between highly charged ions and neutral atoms and molecules. *J. Phys.: Conf. Ser.*, *163*, 012052. https://doi.org/10.1088/1742-6596/163/1/012052

Cappelluti, N., Li, Y. X., Ricarte, A., Agarwal, B., Allevato, V., Ananna, T. T., Ajello, M., Civano, F., Comastri, A., … Urry, C. M. (2017). The *Chandra* COSMOS legacy survey: energy spectrum of the cosmic X-ray background and constraints on undetected populations. *Astrophys. J.*, *837*(1), 19. https://doi.org/10.3847/1538-4357/aa5ea4

Carter, J. A., Sembay, S., and Read, A. M. (2010). A high charge state coronal mass ejection seen through solar wind charge exchange emission as detected by *XMM-Newton*. *Mon. Not. Roy. Astron. Soc.*, *402*(2), 867–878. https://doi.org/10.1111/j.1365-2966.2009.15985.x

Collier, M. R., Abbey, T. F., Bannister, N. P., Carter, J. A., Choi, M., Cravens, T., Evans, M., Fraser, G. W., Hills, H. K., … Travnicek, P. (2009). The lunar X-ray observatory (LXO)/magnetosheath explorer in X-rays (MagEX). *AIP Conf. Proc.*, *1156*(1), 105–111. https://doi.org/10.1063/1.3211802

Collier, M. R., Snowden, S. L., Sarantos, M., Benna, M., Carter, J. A., Cravens, T. E., Farrell, W. M., Fatemi, S., Hills, H. K., … Walsh, B. M. (2014). On lunar exospheric column densities and solar wind access beyond the terminator from ROSAT soft X-ray observations of solar wind charge exchange. *J. Geophys. Res.: Planets*, *119*(7), 1459–1478. https://doi.org/10.1002/2014JE004628

Collier, M. R., Porter, F. S., Sibeck, D. G., Carter, J. A., Chiao, M. P., Chornay, D. J., Cravens, T. E., Galeazzi, M., Keller, J. W., … Walsh, B. M. (2015). Invited article: first flight in space of a wide-field-of-view soft x-ray imager using lobster-eye optics: instrument description and initial flight results. *Rev. Sci. Instrum.*, *86*(7), 071301. https://doi.org/10.1063/1.4927259

Cravens, T. E., Robertson, I. P., and Snowden, S. L. (2001). Temporal variations of geocoronal and heliospheric X-ray emission associated with the solar wind interaction with neutrals. *J. Geophys. Res.: Space Phys.*, *106*(A11), 24883–24892. https://doi.org/10.1029/2000JA000461

Dayeh, M. A., Szalay, J. R., Ogasawara, K., Fuselier, S. A., McComas, D. J., Funsten, H. O., Petrinec, S. M., Schwadron, N. A., and Zirnstein, E. J. (2020). First global images of ion energization in the terrestrial foreshock by the interstellar boundary explorer. *Geophys. Res. Lett.*, *47*(16), e2020GL088188. https://doi.org/10.1029/2020GL088188

Dennerl, K. (2002). Discovery of X-rays from Mars with Chandra. *A&A*, *394*(3), 1119–1128. https://doi.org/10.1051/0004-6361:20021116

Dennerl, K., Burwitz, V., Englhauser, J., Lisse, C., and Wolk, S. (2002). X-rays from Venus discovered with Chandra. In E. M. Schlegel, et al. (Eds.), *The High Energy Universe at Sharp Focus*: *Chandra Science* (pp. 21). San Francisco: Astronomical Society of the Pacific.

Dungey, J. W. (1961). Interplanetary magnetic field and the auroral zones. *Phys. Rev. Lett.*, *6*(2), 47–48. https://doi.org/10.1103/PhysRevLett.6.47

Dunn, W. R., Ness, J. U., Lamy, L., Tremblay, G. R., Branduardi-raymont, G., Snios, B., Kraft, R. P., Yao, Z., and Wibisono, A. D. (2021). A low signal detection of X-rays from Uranus. *J. Geophys. Res.: Space Phys.*, *126*(4), e2020JA028739. https://doi.org/10.1029/2020JA028739

Elsner, R. F., Gladstone, G. R., Waite, J. H., Crary, F. J., Howell, R. R., Johnson, R. E., Ford, P. G., Metzger, A. E., Hurley, K. C., … Weisskopf, M. C. (2002). Discovery of soft X-ray emission from Io, Europa, and the Io plasma torus. *Astrophys. J.*, *572*(2), 1077–1082. https://doi.org/10.1086/340434

Frankel, M., Beiersdorfer, P., Brown, G. V., Gu, M. F., Kelley, R. L., Kilbourne, C. A., and Porter, F. S. (2009). X-ray signature of charge exchange in l-shell sulfur ions. *Astrophys. J.*, *702*(1), 171–177. https://doi.org/10.1088/0004-637X/702/1/171

Galeazzi, M., Chiao, M., Collier, M. R., Cravens, T., Koutroumpa, D., Kuntz, K. D., Lallement, R., Lepri, S. T., McCammon, D., … Walsh, M. (2014). The origin of the local 1/4-keV X-ray flux in both charge exchange and a hot bubble. *Nature*, *512*(7513), 171–173. https://doi.org/10.1038/nature13525

Gilli, R., Comastri, A., and Hasinger, G. (2007). The synthesis of the cosmic X-ray background in the Chandra and XMM-Newton era. *A&A*, *463*(1), 79–96. https://doi.org/10.1051/0004-6361:20066334

Gloeckler, G., Geiss, J., Balsiger, H., Bedini, P., Cain, J. C., Fischer, J., Fisk, L. A., Galvin, A. B., Gliem, F., … Wilken, B. (1992). The solar wind ion composition spectrometer. *Astron. Astrophys. Suppl. Ser.*, *92*(2), 267–289.

Gloeckler, G., and Geiss, J. (2007). The composition of the solar wind in polar coronal holes. *Space Sci. Rev.*, *130*(1-4), 139–152. https://doi.org/10.1007/s11214-007-9189-z

Gosling, J. T., Asbridge, J. R., Bame, S. J., Paschmann, G., and Sckopke, N. (1978). Observations of two distinct populations of bow shock ions in the upstream solar wind. *Geophys. Res. Lett.*, *5*(11), 957–960. https://doi.org/10.1029/GL005i011p00957

Gu, L. Y., Kaastra, J., and Raassen, A. J. J. (2016). Plasma code for astrophysical charge exchange emission at X-ray wavelengths. *A&A*, *588*, A52. https://doi.org/10.1051/0004-6361/201527615

Henley, D. B., Shelton, R. L., and Kuntz, K. D. (2007). An *XMM-Newton* observation of the local bubble using a shadowing filament in the southern galactic hemisphere. *Astrophys. J.*, *661*(1), 304–319. https://doi.org/10.1086/513590

Henley, D. B., and Shelton, R. L. (2008). Comparing *Suzaku* and *XMM-Newton* observations of the soft X-ray background: evidence for solar wind charge exchange emission. *Astrophys. J.*, *676*(1), 335–350. https://doi.org/10.1086/528924

Hietala, H., and Plaschke, F. (2013). On the generation of magnetosheath high-speed jets by bow shock ripples. *J. Geophys. Res.: Space Phys.*, *118*(11), 7237–7245. https://doi.org/10.1002/2013JA019172

Hodges, R. R. Jr. (1994). Monte Carlo simulation of the terrestrial hydrogen exosphere. *J. Geophys. Res.: Space Phys.*, *99*(A12), 23229–23247. https://doi.org/10.1029/94JA02183

Ishi, D., Ishikawa, K., Numazawa, M., Miyoshi, Y., Terada, N., Mitsuda, K., Ohashi, T., … Ezoe, Y. (2019). Suzaku detection of enigmatic geocoronal solar wind charge exchange event associated with coronal mass ejection. *Publ. Astron. Soc. Japan*, *71*(1), 23. https://doi.org/10.1093/pasj/psy142

Jacobsen, K. S., Phan, T. D., Eastwood, J. P., Sibeck, D. G., Moen, J. I., Angelopoulos, V., McFadden, J. P., Engebretson, M. J., Provan, G., … Fornaçon, K. H. (2009). Themis observations of extreme magnetopause

motion caused by a hot flow anomaly. *J. Geophys. Res.: Space Phys.*, *114*(A8), A08210. https://doi.org/10.1029/2008JA013873

Kaaret, P., Zajczyk, A., Larocca, D. M., Ringuette, R., Bluem, J., Fuelberth, W., Gulick, H., Jahoda, K., Johnson, T. E., … Silich, E. M. (2019). *HaloSat*: a CubeSat to study the hot galactic halo. *Astrophys. J.*, *884*(2), 162. https://doi.org/10.3847/1538-4357/ab4193

Kaaret, P., Koutroumpa, D., Kuntz, K. D., Jahoda, K., Bluem, J., Gulick, H., Hodges-Kluck, E., Larocca, D. M., Ringuette, R., and Zajczyk, A. (2020). A disk-dominated and clumpy circumgalactic medium of the Milky Way seen in X-ray emission. *Nat. Astron.*, *4*(11), 1072–1077. https://doi.org/10.1038/s41550-020-01215-w

Kharchenko, V., and Dalgarno, A. (2001). Variability of cometary X-ray emission induced by solar wind ions. *Astrophys. J.*, *554*(1), L99-L102. https://doi.org/10.1086/320929

Koutroumpa, D., Lallement, R., Kharchenko, V., Dalgarno, A., Pepino, R., Izmodenov, V., and Quémerais, E. (2006). Charge-transfer induced EUV and soft X-ray emissions in the heliosphere. *A&A*, *460*(1), 289–300. https://doi.org/10.1051/0004-6361:20065250

Koutroumpa, D. (2007). Etude des émissions gazeuses UV/X et des phénomènes d'échange de charge dans l'Héliosphère : application à des systèmes astrophysiques analogues. Paris: Université Pierre et Marie Curie.

Kraft, R., Markevitch, M., Kilbourne, C., Adams, J. S., Akamatsu, H., Ayromlou, M., Bandler, S. R., Barbera, M., Bennett, D. A., … Vogelsberger, M. (2022). Line Emission Mapper (LEM): probing the physics of cosmic ecosystems. arXiv: 2211.09827.

Kuntz, K. D., Collado-Vega, Y. M., Collier, M. R., Connor, H. K., Cravens, T. E., Koutroumpa, D., Porter, F. S., Robertson, I. P., Sibeck, D. G., … Walsh, B. M. (2015). The solar wind charge-exchange production factor for hydrogen. *Astrophys. J.*, *808*(2), 143. https://doi.org/10.1088/0004-637X/808/2/143

Kuntz, K. D. (2019). Solar wind charge exchange: an astrophysical nuisance. *Astron. Astrophys. Rev.*, *27*(1), 1. https://doi.org/10.1007/s00159-018-0114-0

Leutenegger, M. A., Beiersdorfer, P., Brown, G. V., Kelley, R. L., Kilbourne, C. A., and Porter, F. S. (2010). Measurement of anomalously strong emission from the 1*s*-9*p* transition in the spectrum of H-like phosphorus following charge exchange with molecular hydrogen. *Phys. Rev. Lett.*, *105*(6), 063201. https://doi.org/10.1103/PhysRevLett.105.063201

Leutenegger, M. A., Betancourt-Martinez, G. L., Beiersdorfer, P., Brown, G. V., Kelley, R. L., Kilbourne, C. A., and Porter, F. S. (2013). Charge exchange measurements with an x-ray calorimeter at an electron beam ion trap. *Phys. Scr.*, *2013*(T156), 014006. https://doi.org/10.1088/0031-8949/2013/T156/014006

Lisse, C. M., Dennerl, K., Englhauser, J., Harden, M., Marshall, F. E., Mumma, M. J., Petre, R., Pye, J. P., Ricketts, M. J., … West, R. G. (1996). Discovery of X-ray and extreme ultraviolet emission from comet C/hyakutake 1996 B2. *Science*, *274*(5285), 205-209. https://doi.org/10.1126/science.274.5285.205

Lisse, C. M., McNutt, R. L. Jr., Wolk, S. J., Bagenal, F., Stern, S. A., Gladstone, G. R., Cravens, T. E., Hill, M. E., Kollmann, P., … Ennico, K. A. (2017). The puzzling detection of x-rays from Pluto by *Chandra*. *Icarus*, *287*, 103–109. https://doi.org/10.1016/j.icarus.2016.07.008

Liu, W., Chiao, M., Collier, M. R., Cravens, T., Galeazzi, M., Koutroumpa, D., Kuntz, K. D., Lallement, R., Lepri, S. T., … Walsh, B. M. (2017). The structure of the local hot bubble. *Astrophys. J.*, *834*(1), 33. https://doi.org/10.3847/1538-4357/834/1/33

Ness, J. U., Mewe, R., Schmitt, J. H. M. M., Raassen, A. J. J., Porquet, D., Kaastra, J. S., van der Meer, R. L. J., Burwitz, V., and Predehl, P. (2001). Helium-like triplet density diagnostics. *A&A*, *367*(1), 282–296. https://doi.org/10.1051/0004-6361:20000419

Omidi, N., Blanco-Cano, X., and Russell, C. T. (2005). Macrostructure of collisionless bow shocks: 1. scale lengths. *J. Geophys Res.: Space Phys.*, *110*(A12), A12212. https://doi.org/10.1029/2005JA011169

Paschmann, G., Sckopke, N., Asbridge, J. R., Bame, S. J., and Gosling, J. T. (1980). Energization of solar wind ions by reflection from the earth's bow shock. *J. Geophys. Res.: Space Phys.*, *85*(A9), 4689–4693. https://doi.org/10.1029/JA085iA09p04689

Porquet, D., Dubau, J., and Grosso, N. (2010). He-like ions as practical astrophysical plasma diagnostics: from stellar coronae to active galactic

nuclei. *Space Sci. Rev.*, *157*(1-4), 103–134. https://doi.org/10.1007/s11214-010-9731-2

Rivera, Y. J., Higginson, A., Lepri, S. T., Viall, N. M., Alterman, B. L., Landi, E., Spitzer, S. A., Raines, J. M., Cranmer, S. R., … Dewey, R. M. (2022). Deciphering the birth region, formation, and evolution of ambient and transient solar wind using heavy ion observations. *Front. Astron. Space Sci.*, *9*, 1056347. https://doi.org/10.3389/fspas.2022.1056347

Robertson, I. P., Cravens, T. E., Snowden, S., and Linde, T. (2001). Temporal and spatial variations of heliospheric x-ray emissions associated with charge transfer of the solar wind with interstellar neutrals. *Space Sci. Rev.*, *97*(1-4), 401–405. https://doi.org/10.1023/A:1011822327202

Schwadron, N. A., and Cravens, T. E. (2000). Implications of solar wind composition for cometary X-rays. *Astrophys. J.*, *544*(1), 558–566. https://doi.org/10.1086/317176

Schwartz, S. J., and Burgess, D. (1991). Quasi-parallel shocks: a patchwork of three-dimensional structures. *Geophys. Res. Lett.*, *18*(3), 373–376. https://doi.org/10.1029/91GL00138

Sembay, S., Alme, A. L., Agnolon, D., Arnold, T., Beardmore, A., Belén Balado Margeli, A., Bicknell, C., Bouldin, C., BranduardiRaymont, G., … Yang, S. (2024). The Soft X-ray Imager (SXI) on the SMILE Mission. *Earth Planet. Phys.*, *8*(1), 5–14. https://doi.org/10.26464/epp2023067

Sibeck, D. G., Borodkova, N. L., Schwartz, S. J., Owen, C. J., Kessel, R., Kokubun, S., Lepping, R. P., Lin, R., Liou, K., … Zastenker, G. N. (1999). Comprehensive study of the magnetospheric response to a hot flow anomaly. *J. Geophys. Res.: Space Phys.*, *104*(A3), 4577–4593. https://doi.org/10.1029/1998JA900021

Sibeck, D. G., Allen, R., Aryan, H., Bodewits, D., Brandt, P., Branduardi-Raymont, G., Brown, G., Carter, J. A., Collado-Vega, Y. M., … Wing, S. (2018). Imaging plasma density structures in the soft X-rays generated by solar wind charge exchange with neutrals. *Space Sci. Rev.*, *214*(4), 79. https://doi.org/10.1007/s11214-018-0504-7

Sibeck, D. G., Silveira, M. V. D., and Collier, M. R. (2022). Tracking the subsolar bow shock and magnetopause. *J. Geophys. Res.: Space Phys.*, *127*(9), e2022JA030704. https://doi.org/10.1029/2022JA030704

Smith, R. K., Foster, A. R., and Brickhouse, N. S. (2012). Approximating the X-ray spectrum emitted from astrophysical charge exchange. *Astron. Nachr.*, *333*(4), 301–304. https://doi.org/10.1002/asna.201211673

Smith, R. K., Foster, A. R., Edgar, R. J., and Brickhouse, N. S. (2014). Resolving the origin of the diffuse soft X-ray background. *Astrophys. J.*, *787*(1), 77. https://doi.org/10.1088/0004-637X/787/1/77

Snowden, S. L., Egger, R., Freyberg, M. J., McCammon, D., Plucinsky, P. P., Sanders, W. T., Schmitt, J. H. M. M., Trümper, J., and Voges, W. (1997). ROSAT survey diffuse X-ray background maps II. *Astrophys. J.*, *485*(1), 125–135. https://doi.org/10.1086/304399

Snowden, S. L., Egger, R., Finkbeiner, D. P., Freyberg, M. J., and Plucinsky, P. P. (1998). Progress on establishing the spatial distribution of material responsible for the 1/4 keV soft X-ray diffuse background local and halo components. *Astrophys. J.*, *493*(2), 715–729. https://doi.org/10.1086/305135

Snowden, S. L., Collier, M. R., and Kuntz, K. D. (2004). *XMM-Newton* observation of solar wind charge exchange emission. *Astrophys. J.*, *610*(2), 1182–1190. https://doi.org/10.1086/421841

Tóth, G., Sokolov, I. V., Gombosi, T. I., Chesney, D. R., Clauer, C. R., De Zeeuw, D. L., Hansen, K. C., Kane, K. J., Manchester, W. B., … Kóta, J. (2005). Space weather modeling framework: a new tool for the space science community. *J. Geophys. Res.: Space Phys.*, *110*(9), A12226. https://doi.org/10.1029/2005JA011126

von Steiger, R. and Zurbuchen, T. H. (2016). Solar metallicity derived from in situ solar wind composition. *Astrophys. J.*, *816*(1), 13. https://doi.org/10.3847/0004-637X/816/1/13

Zhang, R. T., Seely, D. G., Andrianarijaona, V. M., Jaeckel, F., Wulf, D., Morgan, K., McCammon, D., and Havener, C. C. (2022). Target and velocity dependence of charge exchange X-ray emission at solar wind velocities. *Astrophys. J.*, *934*(2), 127. https://doi.org/10.3847/1538-4357/ac7b85